PERGAMON

International Journal of Solids and Structures 38 (2001) 4825–4838

INTERNATIONAL JOURNAL OF SOLIDS and STRUCTURES

www.elsevier.com/locate/ijsolstr

SH wave in a transition layer of anisotropy

Kazumi Watanabe [a,*], Kazunari Adachi [b]

[a] *Department of Mechanical Engineering, School of Engineering, Yamagata University, Yonezawa, Yamagata 992-8510, Japan*
[b] *Department of Electrical Engineering and Electronics, School of Engineering, Yamagata University, Yonezawa, Yamagata 992-8510, Japan*

Received 10 December 1999; in revised form 1 August 2000

Abstract

Shear wave, Horizontally polarized wave propagation in an anisotropic elastic medium with non-uniform orientation of the principal axis of anisotropy, which is a good mathematical model of an injection-molded short-fiber reinforced plastic (FRP), is investigated by means of the high frequency approximation. Variations of the phase, ray and power flow density of a plane SH wave are obtained in simple mathematical forms and are graphically illustrated. Wave front patterns are also constructed as an envelope of phase curves. As a result, major wave phenomena in the transition layer with the non-uniform orientation of the principal axis of anisotropy are clarified. The information obtained is found to contribute to further development of the ultrasonic inspection technique for detecting the fiber orientation in the FRP.

Keywords: SH-wave; Off-angled axis of anisotropy; Wave energy; Wave front; FRP

1. Introduction

Injection molded short-fiber-reinforced plastics (FRP) have been widely used in important mechanical elements, such as the cam shafts, in small reciprocal engines and the stationary parts of the automobile transmissions (Tai, 1997). Nevertheless, there still remain some technical problems to be solved in terms of the product design procedure for these types of composite materials, namely those on non-uniform fiber orientation. The fibers in the FRP have the random orientation in general. However, near "weld line" which is formed behind a pin or at the front of two counter flows as shown in Fig. 1, the fiber orientation varies from horizontal to vertical direction along the line, AA′, in the figure. In addition, when a thick (the thickness > 3 mm) FRP plate is molded by injection, the fibers are not uniformly aligned even in a cross-section along the flow direction. Its fiber orientation is almost parallel to the flow direction in the skin layer near the surface, but normal to the direction in the core region as shown in Fig. 1 (b) (Honnma, 1998). Most load applied to the plate is thus supported only by the skin layer, and the inner core has less contribution to

* Corresponding author. Tel.: +81-238-26-3210; fax: +81-238-24-3205.
E-mail addresses: tg111@dip.yz.yamagata-u.ac.jp (K. Watanabe), kadachi@eusluna2.yz.yamagata-u.ac.jp (K. Adachi).

0020-7683/01/$ - see front matter
PII: S0020-7683(00)00307-3

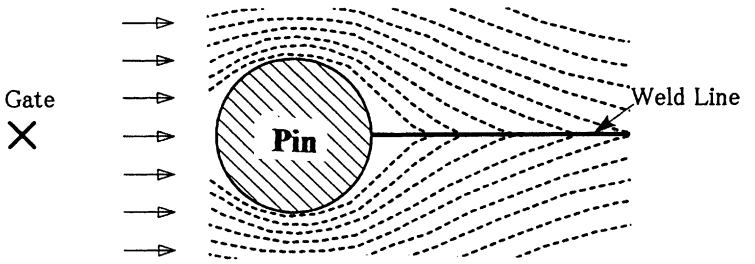

(a) Behind a pin

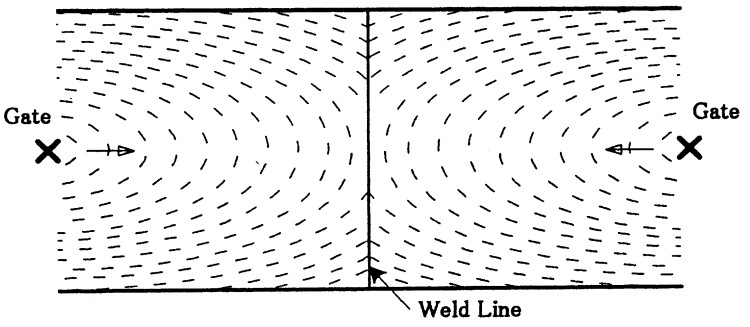

(b) Counter flows from multiple gates

Fig. 1. Schematic fiber orientation in an injection molded FRP: (a) behind a pin and (b) counter flows from multiple gates.

the strength of the plate. The fiber orientation is, therefore, quite an important factor in the production design of the FRP. At present, there is no reliable non-destructive inspection technique for detection of the weld lines or estimation of the skin layer thickness.

There are some methods (Kikuchi and Koyama, 1996) available for computer simulations on these matters, but no practical technique for inspection of the real products. Though a research project has recently started for developing such an ultrasonic inspection technique for the injection-molded FRP (Kuriyama et al., 1997), they have encountered some difficulties in data analysis owing to the lack of the basic knowledge on the wave propagation in the material with this type of anisotropy. Wave analysis in the transition layer of anisotropy is necessary to clarify the phenomenon. However, many works for the wave analysis have previously been done only for the case of the rectilinear principal axis of anisotropy and the information on the wave propagation in the transition layer of anisotropy is quite scarce. Hence, the wave phenomena, especially in the transition region where the orientation of the principal axis of anisotropy drastically changes, should be clarified in order to develop a reliable ultrasonic inspection technique for detection of the weld line and the thickness of the skin layer. This is our motivation of the present work.

Fortunately, the injection-molded FRP can be treated as an anisotropic elastic medium with non-uniform orientation of the principal axis of anisotropy. In the transition layer between the skin layer and the inner core in the FRP plate, the principal axis is considered to rotate from the direction almost parallel to the surface to that normal to it as shown in Fig. 3. The fiber orientation, which is represented as the direction of the principal axis of anisotropy in the mathematical model, is a function of the depth in the transition layer. Rigorous mathematical analysis of the wave propagation in this layer is very difficult.

Thus, as a first step, we consider SH-wave propagation in the transition layer employing the high frequency approximation technique (the ray method). In our analysis, we consider a transition layer sandwiched by two half spaces. One represents the skin layer, and the other the inner core. They are perfectly bonded to the transition layer. Two incident waves propagating into the transition layer are considered, namely; the wave coming from the skin layer and the one from the inner core. Our focus of interest is placed on the basic wave properties, namely the phase, ray, power flow density and wave front patterns of the SH waves in the transition layer.

2. Formulation of problem

Rigorous mathematical treatment of wave propagation in the injection molded FRP is very difficult. In order to discuss effects of variable fiber orientation on wave propagation, we have to introduce some assumptions for the sake of the simplification. The first assumption is that the fiber orientation is variable only on a plane and constant along normal direction to the plane. The second one is that the fiber is very small in length and its orientation is continuously changing on the plane. With these assumptions, we can introduce a local Cartesian coordinates system (X, Y, Z) attached to one fiber in the FRP (we call it a "fiber point" hereafter), as shown in Fig. 2. All fibers in the FRP are laid on the X–Y plane, such that the fiber orientation at the fiber point coincides with the X-axis, and the orientation is constant along the Z-axis. As the third assumption, there is no volumetric change of the fibers in the entire region of the FRP. Thus, if we estimate the elastic modulus at a fiber point, Hooke's law at this fiber point is valid all over the region within a frame of the local coordinates system.

Now, we can consider that the FRP is an orthotropic material and its elastic response is governed by the form of

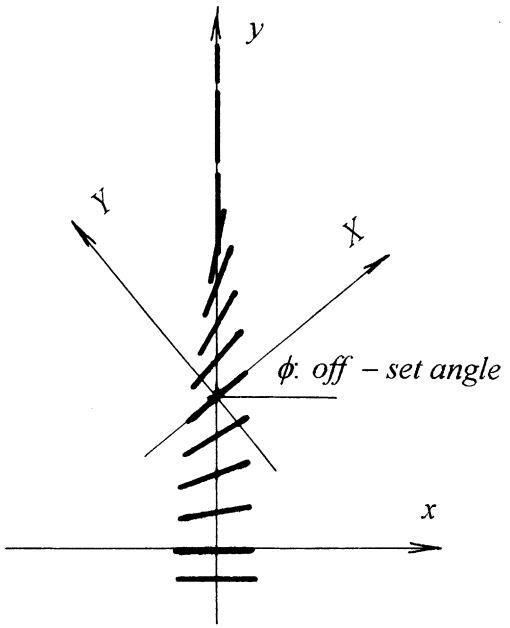

Fig. 2. Local and global coordinates systems.

$$\begin{bmatrix} \sigma_{XX} \\ \sigma_{YY} \\ \sigma_{ZZ} \\ \sigma_{XY} \\ \sigma_{YZ} \\ \sigma_{ZX} \end{bmatrix} = \begin{bmatrix} C_{11} & C_{12} & C_{13} & 0 & 0 & 0 \\ C_{12} & C_{22} & C_{23} & 0 & 0 & 0 \\ C_{13} & C_{23} & C_{33} & 0 & 0 & 0 \\ 0 & 0 & 0 & C_{44} & 0 & 0 \\ 0 & 0 & 0 & 0 & C_{55} & 0 \\ 0 & 0 & 0 & 0 & 0 & C_{66} \end{bmatrix} \begin{bmatrix} \varepsilon_{XX} \\ \varepsilon_{YY} \\ \varepsilon_{ZZ} \\ \varepsilon_{XY} \\ \varepsilon_{YZ} \\ \varepsilon_{ZX} \end{bmatrix}, \tag{1}$$

where C_{ij} are elastic constants.

Since the fiber orientation is constant along the Z-axis, we can decompose a two-dimensional deformation into in- and anti-plane deformations. In order to discuss SH-wave propagation in the FRP, we consider the anti-plane deformation. Then, $u_Z(X, Y, t)$ is the only non-zero component of the displacement and Hooke's law can be reduced as

$$\begin{bmatrix} \sigma_{YZ} \\ \sigma_{ZX} \end{bmatrix} = \begin{bmatrix} C_{55} & 0 \\ 0 & C_{66} \end{bmatrix} \begin{bmatrix} \varepsilon_{YZ} \\ \varepsilon_{ZX} \end{bmatrix}. \tag{2}$$

Now, let us transform the local coordinates system (X, Y) attached to a fiber point to the global coordinates system (x, y) as shown in Figs. 2 and 3. Let ϕ denote an off-set angle of the fiber orientation measured from the global x-axis, Hooke's law of Eq. (2) is also transformed to

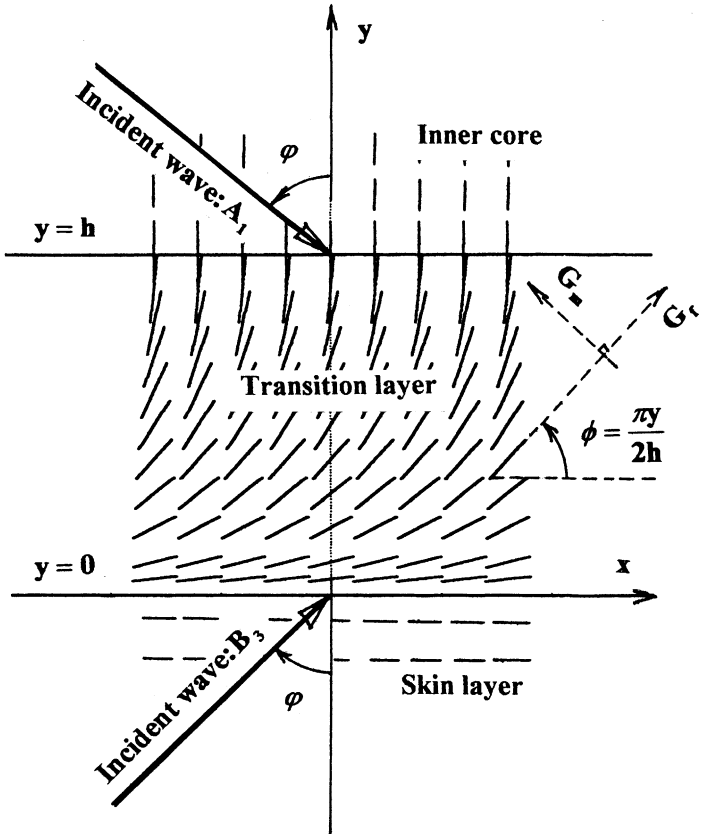

Fig. 3. A transition layer sandwiched by the skin layer and the inner core.

$$\begin{bmatrix}\sigma_{xz}\\ \sigma_{yz}\end{bmatrix}=\begin{bmatrix}\cos\phi & -\sin\phi\\ \sin\phi & \cos\phi\end{bmatrix}\begin{bmatrix}C_{66} & 0\\ 0 & C_{55}\end{bmatrix}\begin{bmatrix}\cos\phi & \sin\phi\\ -\sin\phi & \cos\phi\end{bmatrix}\begin{bmatrix}\varepsilon_{xz}\\ \varepsilon_{yz}\end{bmatrix}. \tag{3}$$

As we consider wave propagation in the transition layer sandwiched by two half spaces, the region of analysis is decomposed into three sub-regions, namely Region 1: the "inner core" ($h < y$), Region 2: the "transition" layer ($0 < y < h$), Region 3: the "skin" layer ($y < 0$), as shown in Fig. 3. Super- or sub-script $j(=1, 2, 3)$ denote the sub-regions. In the transition layer, the off-set angle from the x-axis is varying from $\phi = 0$ to $\pi/2$. We assume that the off-set angle at each fiber point is in proportion to the layer depth y, as

$$\phi = \pi y/(2h); \quad 0 \leqslant \phi \leqslant \pi/2. \tag{4}$$

Consequently, Hooke's law in the transition layer is given by the simple form:

$$\begin{bmatrix}\sigma_{xz}^{(2)}\\ \sigma_{yz}^{(2)}\end{bmatrix}=\begin{bmatrix}G_f\cos^2\phi+G_m\sin^2\phi & (G_f-G_m)\sin\phi\cos\phi\\ (G_f-G_m)\sin\phi\cos\phi & G_f\sin^2\phi+G_m\cos^2\phi\end{bmatrix}\begin{bmatrix}u_{z,x}^{(2)}\\ u_{z,y}^{(2)}\end{bmatrix}, \tag{5}$$

where $G_m = C_{55}$ and $G_f = C_{66}$, and we denote that $u_z^{(j)}$ as the anti-plane displacement. Eq. (5) can also be applied to the skin layer with zero off-set angle by letting $\phi = 0$ and $j = 3$, and to the inner core with $\phi = \pi/2$ and $j = 1$. As we consider the anti-plane deformation for SH wave propagation, equation of motion in each sub-region is given by the form:

$$\sigma_{xz,x}^{(j)} + \sigma_{yz,y}^{(j)} = \rho u_{z,tt}^{(j)}, \quad j = 1, 2, 3. \tag{6}$$

For the boundary condition at two interfaces: $y = 0, h$, we employ the condition of perfect bonding.

3. High frequency approximation

Now, we introduce dimensionless variables:

$$\xi = \frac{\pi x}{h}, \quad \eta = \frac{\pi y}{h}, \quad \tau = \frac{\pi c_0 t}{h}, \tag{7}$$

and material parameters:

$$\varepsilon = \frac{1-v}{1+v}, \qquad v = \frac{1-\varepsilon}{1+\varepsilon} = \frac{G_m}{G_f}, \qquad c_0 = \sqrt{\frac{(G_f+G_m)/2}{\rho}}. \tag{8}$$

The displacement equation of motion and Hooke's law in the transition layer are

$$(1+\varepsilon\cos\eta)u_{z,\xi\xi}^{(2)} + 2\varepsilon\sin\eta u_{z,\xi\eta}^{(2)} + (1-\varepsilon\cos\eta)u_{z,\eta\eta}^{(2)} + \varepsilon\cos\eta u_{z,\xi}^{(2)} + \varepsilon\sin\eta u_{z,\eta}^{(2)} = u_{z,\tau\tau}^{(2)}, \tag{9}$$

$$\begin{bmatrix}\sigma_{xz}^{(2)}\\ \sigma_{yz}^{(2)}\end{bmatrix}=\frac{\pi\mu_0}{h}\begin{bmatrix}1+\varepsilon\cos\eta & \varepsilon\sin\eta\\ \varepsilon\sin\eta & 1-\varepsilon\cos\eta\end{bmatrix}\begin{bmatrix}u_{z,\xi}^{(2)}\\ u_{z,\eta}^{(2)}\end{bmatrix}. \tag{10}$$

The similar equations,

$$(1-\varepsilon)u_{z,\xi\xi}^{(1)} + (1+\varepsilon)u_{z,\eta\eta}^{(1)} = u_{z,\tau\tau}^{(1)}, \tag{11}$$

$$\begin{bmatrix}\sigma_{xz}^{(1)}\\ \sigma_{yz}^{(1)}\end{bmatrix}=\frac{\pi\mu_0}{h}\begin{bmatrix}1-\varepsilon & 0\\ 0 & 1+\varepsilon\end{bmatrix}\begin{bmatrix}u_{z,\xi}^{(1)}\\ u_{z,\eta}^{(1)}\end{bmatrix}, \tag{12}$$

are given for the inner core, and

$$(1+\varepsilon)u^{(3)}_{z\ ,\xi\xi}+(1-\varepsilon)u^{(3)}_{z\ ,\eta\eta}=u^{(3)}_{z\ ,\tau\tau}, \tag{13}$$

$$\begin{bmatrix}\sigma^{(3)}_{xz}\\ \sigma^{(3)}_{yz}\end{bmatrix}=\frac{\pi\mu_0}{h}\begin{bmatrix}1+\varepsilon & 0\\ 0 & 1-\varepsilon\end{bmatrix}\begin{bmatrix}u^{(3)}_{z\ ,\xi}\\ u^{(3)}_{z\ ,\eta}\end{bmatrix}, \tag{14}$$

for the skin layer.

A time harmonic wave with the dimensionless frequency ω and the wave number κ is expressed by

$$u^{(j)}_z=W_j(\eta)\exp\{\mathrm{i}\omega(\tau-\kappa\xi)\},\quad j=1,2,3. \tag{15}$$

Here, the dimensionless frequency ω is related to the actual frequency ϖ by $\omega=h\varpi/(\pi c_0)$. Substituting Eq. (15) into Eqs. (9), (11) and (13), we have ordinary differential equations for displacement amplitude $W_j(\eta)$. For amplitude $W_2(\eta)$ in the transition layer, we have a complicated equation as

$$(1-\varepsilon\cos\eta)W_2''(\eta)+(1-2\mathrm{i}\kappa\omega)\varepsilon\sin\eta W_2'(\eta)+[\omega^2\{1-\kappa^2(1+\varepsilon\cos\eta)\}-\mathrm{i}\varepsilon\kappa\omega\cos\eta]W_2(\eta)=0. \tag{16}$$

It is very difficult to get an exact solution of the above Eq. (16), but possible to obtain an approximate solution using the high frequency approximation (Cerveny and Ravindra, 1971). The approximate solution is expressed in the series form of inverse power of frequency as

$$W_2(\eta)=\{F(\eta)+\mathrm{O}(\omega^{-1})\}\exp\{\mathrm{i}\omega g(\eta)\}. \tag{17}$$

Substitute this equation into Eq. (16), and equate the same power of frequency, the Eikonal equation:

$$(1-\varepsilon\cos\eta)\{g'(\eta)\}^2-2\kappa\varepsilon\sin\eta g'(\eta)-\{1-\kappa^2(1+\varepsilon\cos\eta)\}=0, \tag{18}$$

is obtained from the highest order, $\mathrm{O}(\omega^2)$, and the amplitude equation:

$$2\{(1-\varepsilon\cos\eta)g'(\eta)-\kappa\varepsilon\sin\eta\}F'(\eta)+[\{(1-\varepsilon\cos\eta)g'(\eta)\}'-\kappa\varepsilon\cos\eta]F(\eta)=0, \tag{19}$$

from $\mathrm{O}(\omega^1)$. The solutions of Eqs. (18) and (19) are given by

$$g(\eta)=\kappa\log(1-\varepsilon\cos\eta)\pm\int^{\eta}\frac{\sqrt{(1-\varepsilon\cos\eta)-\kappa^2(1-\varepsilon^2)}}{1-\varepsilon\cos\eta}\,\mathrm{d}\eta, \tag{20}$$

$$F(\eta)=\{(1-\varepsilon\cos\eta)-\kappa^2(1-\varepsilon^2)\}^{-1/4}. \tag{21}$$

Then, we have the approximate amplitude in the transition layer:

$$W_2(\eta)\approx\frac{\exp\{\mathrm{i}\omega\kappa\log(1-\varepsilon\cos\eta)\}}{\sqrt{\beta_2(\eta)}}\left[A_2\exp\left\{+\mathrm{i}\omega\int_0^{\eta}\frac{\beta_2(\eta)}{1-\varepsilon\cos\eta}\mathrm{d}\eta\right\}+B_2\exp\left\{-\mathrm{i}\omega\int_0^{\eta}\frac{\beta_2(\eta)}{1-\varepsilon\cos\eta}\mathrm{d}\eta\right\}\right]. \tag{22}$$

We use the above equation as the solution in the transition layer. However, it should be noted that the terms of $\mathrm{O}(\omega^{-1})$ in Eq. (17) is neglected and the approximate solution is valid only for the high frequency region. This is because we have neglected the terms of $\mathrm{O}(\omega^0)$ in the differential equation (16). The other restriction is $\beta_2\neq 0$. This states that the approximate solution is not valid at a turning point of ray.

Two other solutions for the skin layer and the inner core can be exactly obtained as

$$W_3(\eta)=A_3\exp(+\mathrm{i}\omega\beta_3\eta)+B_3\exp(-\mathrm{i}\omega\beta_3\eta), \tag{23}$$

for the skin layer, and

$$W_1(\eta)=A_1\exp\{+\mathrm{i}\omega\beta_1(\eta-\pi)\}+B_1\exp\{-\mathrm{i}\omega\beta_1(\eta-\pi)\}, \tag{24}$$

for the inner core, where

$$\beta_1 = \sqrt{\frac{1-(1-\varepsilon)\kappa^2}{1+\varepsilon}}, \qquad \beta_2(\eta) = \sqrt{1-\varepsilon\cos\eta-(1-\varepsilon^2)\kappa^2}, \qquad \beta_3 = \sqrt{\frac{1-(1+\varepsilon)\kappa^2}{1-\varepsilon}}. \tag{25}$$

In the above three Eqs. (22)–(24), coefficients A_j and B_j are unknown. However, when we consider the incident wave coming from the skin layer or the inner core, coefficients B_3 and A_1 should be the known.

Applying the continuity conditions at two interfaces,

$$\begin{aligned} \left[\sigma_{yz}^{(2)}-\sigma_{yz}^{(3)}\right] &= \left[u_z^{(2)}-u_z^{(3)}\right] = 0, \quad y=0, \\ \left[\sigma_{yz}^{(1)}-\sigma_{yz}^{(2)}\right] &= \left[u_z^{(1)}-u_z^{(2)}\right] = 0, \quad y=h, \end{aligned} \tag{26}$$

we have for displacement amplitudes $W_j(\eta)$ as

$$\begin{aligned} W_1(\eta) = A_1\exp\{+\mathrm{i}\omega\beta_1(\eta-\pi)\} + B_3\sqrt{\frac{\beta_2(0)}{\beta_2(\pi)}}\exp\left\{\mathrm{i}\omega\kappa\log\left(\frac{1+\varepsilon}{1-\varepsilon}\right) - \mathrm{i}\omega\beta_1(\eta-\pi)\right. \\ \left. -\mathrm{i}\omega\int_0^{\pi}\frac{\beta_2(\eta)}{1-\varepsilon\cos\eta}\mathrm{d}\eta\right\}, \end{aligned} \tag{27}$$

$$\begin{aligned} W_2(\eta) = A_1\sqrt{\frac{\beta_2(\pi)}{\beta_2(\eta)}}\exp\left\{-\mathrm{i}\omega\kappa\log\left(\frac{1+\varepsilon}{1-\varepsilon\cos\eta}\right) - \mathrm{i}\omega\int_{\eta}^{\pi}\frac{\beta_2(\eta)}{1-\varepsilon\cos\eta}d\eta\right\} \\ + B_3\sqrt{\frac{\beta_2(0)}{\beta_2(\eta)}}\exp\left\{+\mathrm{i}\omega\kappa\log\left(\frac{1-\varepsilon\cos\eta}{1-\varepsilon}\right) - \mathrm{i}\omega\int_0^{\eta}\frac{\beta_2(\eta)}{1-\varepsilon\cos\eta}\mathrm{d}\eta\right\}, \end{aligned} \tag{28}$$

$$W_3(\eta) = A_1\sqrt{\frac{\beta_2(\pi)}{\beta_2(0)}}\exp\left\{-\mathrm{i}\omega\kappa\log\left(\frac{1+\varepsilon}{1-\varepsilon}\right) + \mathrm{i}\omega\beta_3\eta - i\omega\int_0^{\pi}\frac{\beta_2(\eta)}{1-\varepsilon\cos\eta}\mathrm{d}\eta\right\} + B_3\exp\{-\mathrm{i}\omega\beta_3\eta\}. \tag{29}$$

In Eq. (27), the first term with coefficient A_1 is the incident wave in the inner core and the second term with coefficient B_3 is the transmitted wave coming from the skin layer. Similarly, in Eq. (29), the term with B_3 gives the incident wave and that with A_1 gives the transmitted wave from the inner core. The term with coefficient A_1 in Eq. (28) is the transmitted wave coming from the inner core and that with B_3 is also the transmitted wave from the skin layer. It should be noted that no reflected wave terms are in these equations, since the axis of anisotropy and all material parameters are continuous across the two interfaces: $y=0$ and h. Then, the wave does not reflect at these interfaces and all wave energy passes through the interfaces.

4. Incident wave from the skin layer

When the incident wave is coming from the skin layer with amplitude B_3 and the incident angle φ as defined in Fig. 3, the wave number κ is given by

$$\kappa = \frac{\tan\varphi}{\sqrt{1+\varepsilon}\sqrt{v+\tan^2\varphi}}. \tag{30}$$

In this case, the both, β_1 and $\beta_2(\eta)$, are real for all η and the incident angle φ. Then, all transmitted wave in the transition layer can reach to the inner core without turning.

In order to derive the power flow density, we extract the real part from the term with coefficient B_3 in Eq. (28). The displacement in the transition layer is

$$u_z^{(2)} = B_3\sqrt{\frac{\beta_2(0)}{\beta_2(\eta)}}\cos\left[\omega\left\{\tau - \kappa\xi + \kappa\log\left(\frac{1-\varepsilon\cos\eta}{1-\varepsilon}\right) - \int_0^{\eta}\frac{\beta_2(\eta)}{1-\varepsilon\cos\eta}\mathrm{d}\eta\right\}\right]. \tag{31}$$

Phase and ray curves are easily obtained from the argument in the above cosine function. They are

$$Phase: \xi(\eta) = \log\left(\frac{1-\varepsilon\cos\eta}{1-\varepsilon}\right) - \frac{1}{\kappa}\int_0^{\eta}\frac{\beta_2(\eta)}{1-\varepsilon\cos\eta}\mathrm{d}\eta + \frac{\tau}{\kappa}, \tag{32}$$

$$Ray: \xi(\eta) = \kappa\int_0^{\eta}\frac{1-\varepsilon\cos\eta}{\beta_2(\eta) - \kappa\varepsilon\sin\eta}\mathrm{d}\eta. \tag{33}$$

The phase plane of the incident wave in the skin layer is flat. However, as given by Eq. (32), the phase plane of the transmitted wave in the transition layer is curved, because of continuous variation of the principal axis of anisotropy. The ray trajectory of the transmitted wave is also curved. The variations of the phase and ray in the transition layer are shown in Fig. 4(a) and (b). These figures illustrate that the ray with the positive incident angle, φ, bends with increase in the incident angle. When the ray has the negative incident angle, it is almost straight. This means that waves in the anisotropic medium are dragged into a direction of the greater elastic modulus. In order to make this effect clear, wave energy should be discussed.

The power flow density through a plane normal to the vector, $\mathbf{n} = (n_x, n_y)$, is defined as

$$P_j(\eta;\psi) = \frac{\varpi}{2\pi}\int_0^{2\pi/\varpi}\left(\sigma_{xz}^{(j)}n_x + \sigma_{yz}^{(j)}n_y\right)\frac{\partial u_z^{(j)}}{\partial t}\mathrm{d}t. \tag{34}$$

If we define the energy flow direction ψ_j as $(n_x, n_y) = (\sin\psi_j, \cos\psi_j)$ in each region, the maximum power flow density in the skin layer can be expressed by

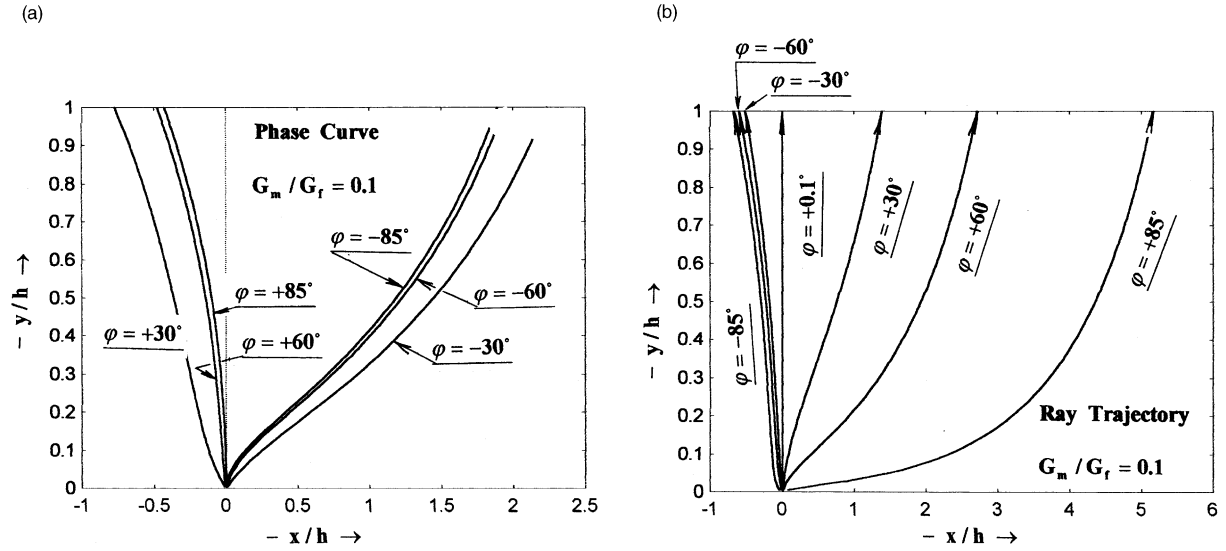

Fig. 4. Phase curve and ray in the transition layer (incident wave is coming from the lower skin layer): (a) phase curve and (b) ray.

$$P_3 = \frac{\mu_0 c_0}{2}\sqrt{1+\varepsilon}\left(\frac{\pi\omega}{h}B_3\right)^2\sqrt{\frac{v^2+\tan^2\varphi}{v+\tan^2\varphi}}, \tag{35}$$

and its flow direction is

$$\psi_3 = \tan^{-1}\left(\frac{\tan\varphi}{v}\right). \tag{36}$$

The maximum power flow density in the transition layer is also given by

$$P_2(\eta) = \frac{\mu_0 c_0}{2}\left(\frac{\pi\omega}{h}B_3\right)^2\frac{\beta_2(0)}{\beta_2(\eta)}\frac{\sqrt{\{(1-\varepsilon^2)\kappa+\varepsilon\beta_2(\eta)\sin\eta\}^2+\{(1-\varepsilon\cos\eta)\beta_2(\eta)\}^2}}{1-\varepsilon\cos\eta}, \tag{37}$$

and its flow direction is

$$\psi_2(\eta) = \tan^{-1}\left\{\frac{1-\varepsilon^2}{1-\varepsilon\cos\eta}\frac{\kappa}{\beta_2(\eta)}+\frac{\varepsilon\sin\eta}{1-\varepsilon\cos\eta}\right\}. \tag{38}$$

Fig. 5(a) shows variation of the power flow density with the depth η in the transition layer. The power flow density is changing its magnitude drastically near the skin layer. However, at the inner core, where the fiber orientation is normal to the layer, the power flow direction is parallel to that of the fiber. In particular, when the incident angle is zero or close to zero ($\varphi \approx 0$), it has the maximum value at a depth. To show these visually, the power flow density on a ray is computed. The arrows in Fig. 5(b) and (c) show the magnitude of the power flow density at a point on the ray.

5. Incident wave from the inner core

When an incident wave with the amplitude A_1 is coming from the inner core, its wave number is given by

$$\kappa = \frac{\tan\varphi}{\sqrt{1+\varepsilon}\sqrt{1+v\tan^2\varphi}}. \tag{39}$$

The phase and ray curves in the transition layer are given by

$$\textit{Phase}: \xi(\eta) = \log\left(\frac{1-\varepsilon\cos\eta}{1+\varepsilon}\right) - \frac{1}{\kappa}\int_\eta^\pi \frac{\beta_2(\eta)}{1-\varepsilon\cos\eta}\mathrm{d}\eta + \frac{\tau}{\kappa}, \tag{40}$$

$$\textit{Ray}: \xi(\eta) = \kappa\int_\eta^\pi \frac{1-\varepsilon\cos\eta}{\beta_2(\eta)+\kappa\varepsilon\sin\eta}\mathrm{d}\eta. \tag{41}$$

In this case, $\beta_2(\eta)$ becomes pure imaginary in a region of η in the transition layer. The solution of Eq. (28) is valid:

(1) if $0 \leqslant \varphi < \tan^{-1}(1/\sqrt{1-v})$, the transmitted wave can reach to the skin layer.

(2) if $\tan^{-1}(1/\sqrt{1-v}) < \varphi$ and $\eta_c \leqslant \eta < \pi$, where

$$\eta_c = 2\sin^{-1}\left\{\sqrt{\frac{\tan^2\varphi - 1/(1-v)}{\tan^2\varphi + 1/v}}\right\}. \tag{42}$$

The transmitted wave turns at $\eta = \eta_c$ and then goes back to the inner core.

Fig. 6(a) and (b) show the phase curve and ray trajectory for a limited range of incident angle, $0 < |\varphi| < \tan^{-1}(1/\sqrt{1-v})$ within which the ray does not turn and reach the skin layer.

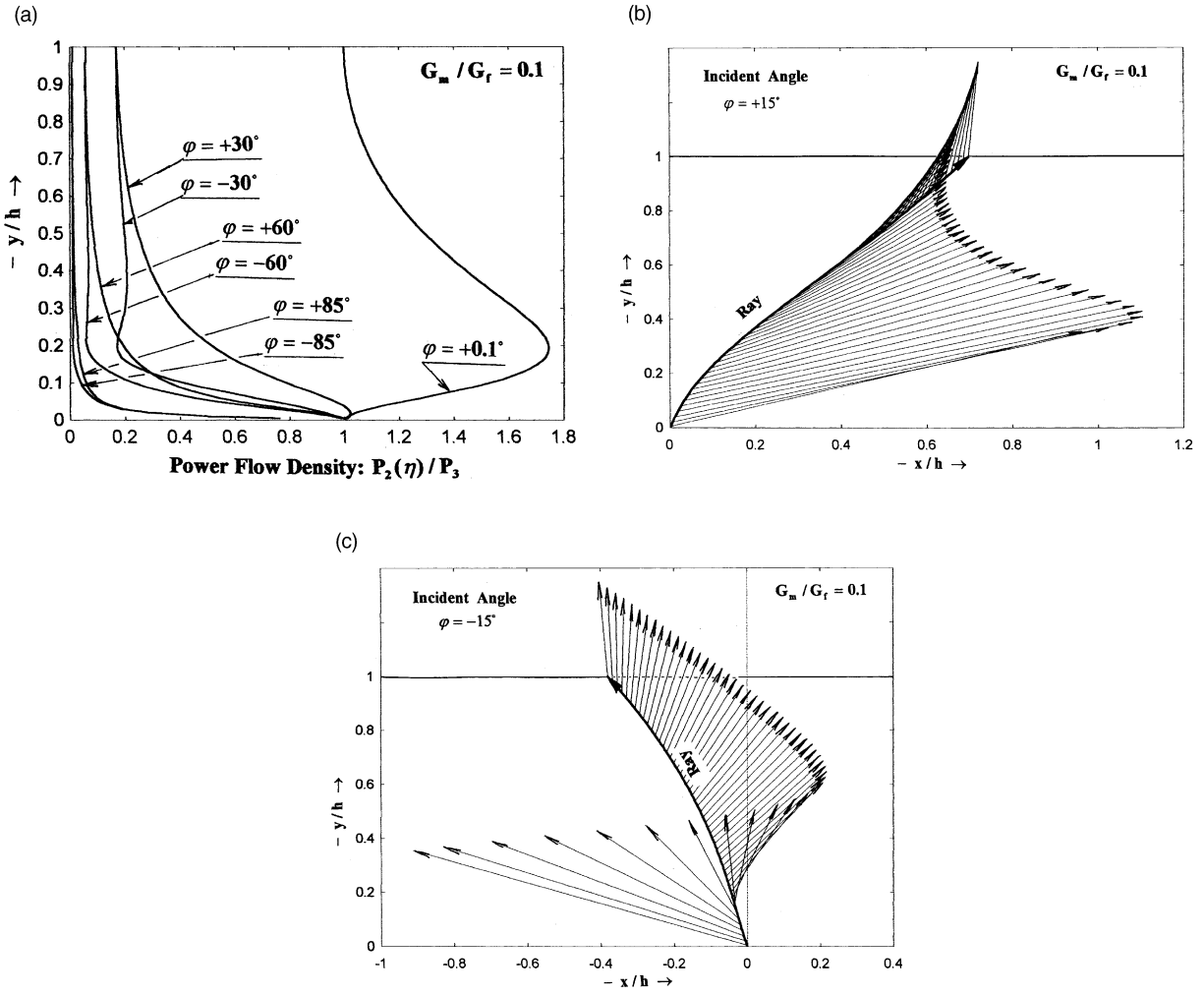

Fig. 5. The maximum power flow density in the transition layer: (a) variation with depth, (b) power flow density on a ray (positive incident angle) and (c) power flow density on a ray (negative incident angle).

The maximum power flow density of the incident wave in the inner core is given by

$$P_1 = \frac{\mu_0 c_0}{2}\left(\frac{\pi\omega}{h}A_1\right)^2 \sqrt{\frac{(1-\varepsilon)(1+v^2\tan^2\varphi)}{1+v\tan^2\varphi}}, \tag{43}$$

and its flow direction is

$$\psi_1 = \tan^{-1}(v\tan\varphi). \tag{44}$$

Then, the power flow density and its flow direction in the transition layer are given by

$$P_2(\eta) = \frac{\mu_0 c_0}{2}\left(\frac{\pi\omega}{h}A_1\right)^2 \frac{\beta_2(\pi)}{\beta_2(\eta)} \frac{\sqrt{\{(1-\varepsilon^2)\kappa - \varepsilon\beta_2(\eta)\sin\eta\}^2 + \{(1-\varepsilon\cos\eta)\beta_2(\eta)\}^2}}{1-\varepsilon\cos\eta}, \tag{45}$$

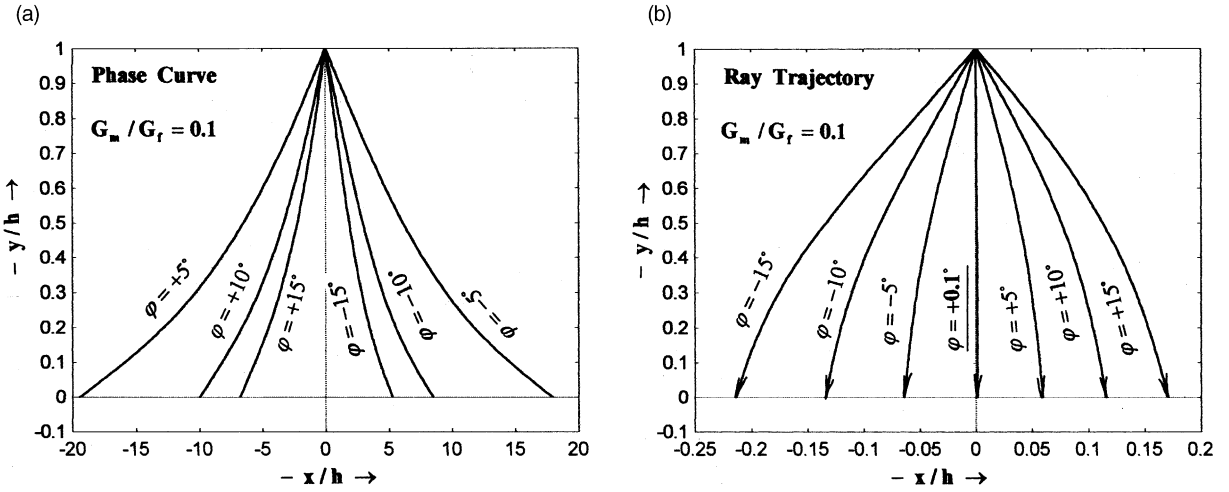

Fig. 6. Phase curve and ray in the transition layer (incident wave is coming from the upper core): (a) phase curve and (b) ray.

$$\psi_2(\eta) = \tan^{-1}\left\{ \frac{1-\varepsilon^2}{1-\varepsilon\cos\eta}\frac{\kappa}{\beta_2(\eta)} - \frac{\varepsilon\sin\eta}{1-\varepsilon\cos\eta} \right\}. \tag{46}$$

Fig. 7(a) shows variation of the power flow density with the depth η in the layer. Though the incident angle is small, the power flow density is changing its magnitude drastically near the lower interface. Fig. 7(b) and (c) show the power flow density on a ray. The arrows in the figures show the magnitude and direction of the power flow density at the depth on the ray.

6. Wave front curve

Since we have employed the high frequency approximation, it is possible to construct a wave front curve. Using phase curve equation (32), the time evolution of wave front pattern from a point source placed at the coordinates origin (0, 0) is constructed as an envelope of phase curves. Fig. 8 show these for two parameters, $v = 0.5$ and 0.05. The wave front curve at the initial time is nearly elliptic and then gets deformed as the time goes. The evolution from the elliptic curve is more affected when the anisotropy is stronger. The deformed edge, we call it the "deepest point" in the transition layer, can be derived analytically from the phase curve equation (32) with zero incident angle $\varphi = 0$. The deepest point (ξ^*, η^*) on the wave front in the transition layer is given by

$$\xi^* = \log\left(\frac{1-\varepsilon\cos\eta^*}{1-\varepsilon}\right), \tag{47}$$

where η^* is a solution of the transcendental equation:

$$\tau - \int_0^{\eta^*} \frac{1}{\sqrt{1-\varepsilon\cos\eta}}\mathrm{d}\eta = 0. \tag{48}$$

The integral in the above equation can be evaluated in terms of elliptic integrals. Then, Eq. (39) is rewritten by

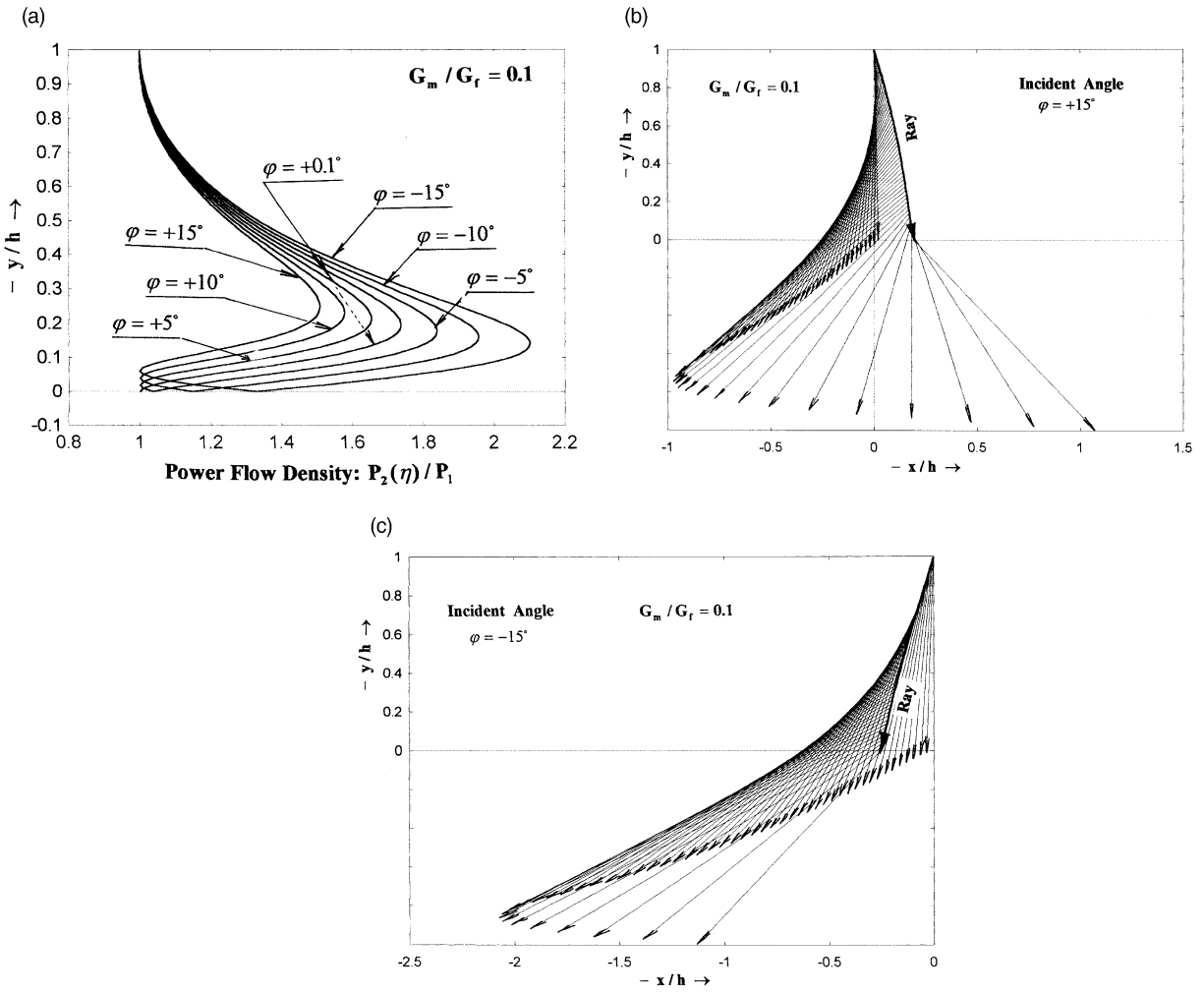

Fig. 7. The maximum power flow density in the transition layer: (a) variation with depth, (b) power flow density on a ray (positive incident angle), and (c) power flow density on a ray (negative incident angle).

$$\tau - \frac{2}{\sqrt{1+\varepsilon}}\left\{K\left(\sqrt{\frac{2\varepsilon}{1+\varepsilon}}\right) - F\left(\sin^{-1}(\cos(\eta^*/2)), \sqrt{\frac{2\varepsilon}{1+\varepsilon}}\right)\right\} = 0, \tag{49}$$

where $K(x)$ and $F(\phi, x)$ are the complete and incomplete elliptic integrals.

The first touch of the wave front at the upper edge of the transition layer is at the time

$$\tau = \frac{2}{\sqrt{1+\varepsilon}} K\left(\sqrt{\frac{2\varepsilon}{1+\varepsilon}}\right), \tag{50}$$

and its horizontal shift is

$$\xi^* = -\log(v). \tag{51}$$

These are shown in Fig. 9.

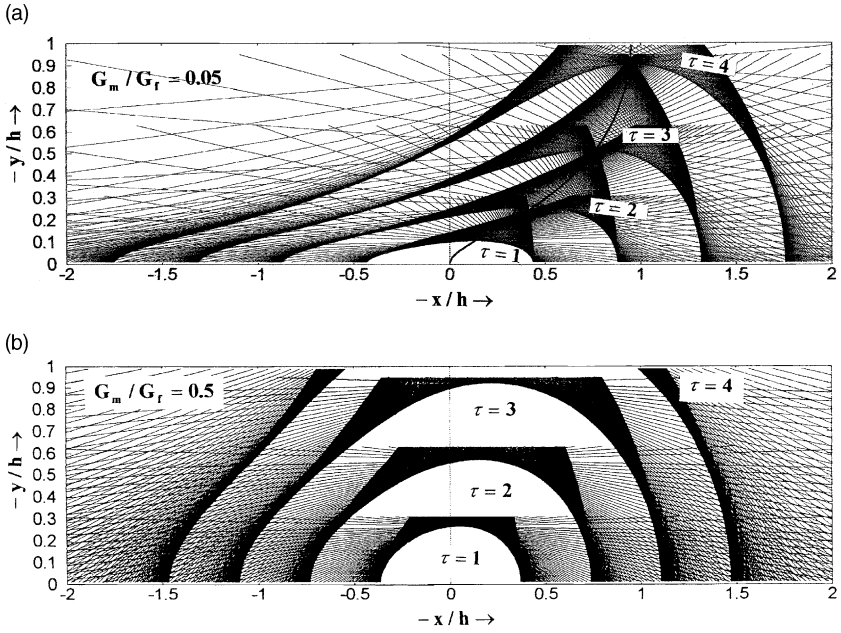

Fig. 8. Construction of wave front curve in the transition layer: (a) $G_m/G_f = 0.05$ and (b) $G_m/G_f = 0.5$.

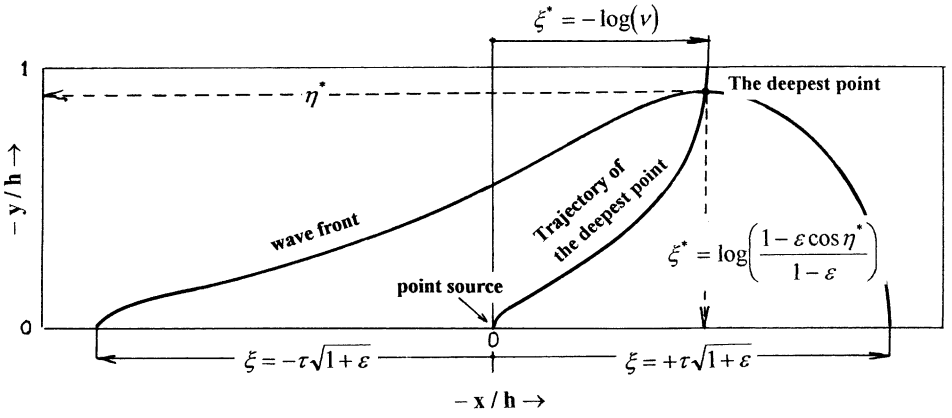

Fig. 9. The deepest point on a wave front in the transition layer.

7. Conclusion

Characteristics of SH wave in an anisotropic elastic medium with variable off-set angle of the principal axis of anisotropy is considered as a model of injection-molded FRP. Employing the high frequency approximation, the phase and ray curves, power flow density and wave front patterns are discussed and are illustrated.

It should be mentioned that the direction and magnitude of the wave energy are changing drastically near the skin layer, not near the inner core. Wave front curve originated at the coordinates origin gets deformed and dragged into the fiber direction, as the time goes.

The results are instructive for experimentalists. However, in the present work, the case of wave turning is not considered. This is left to our future work.

Acknowledgements

The authors wishes to express their thanks to referees for helpful comments in the revision of our paper.

References

Cerveny, V., Ravindra, R., 1971. Theory of Seismic Head Waves. University of Toronto Press.
Kikuchi, H., Koyama, K., 1996. The relation between thickness and warpage in a disk injection molded fiber reinforced PA66. Polym. Engng. Sci. 36 (10), 1317–1325.
Kuriyama, T., et al. 1997. private communications.
Homma, S., 1998. Fiber orientation and its control for the injection molded FRP. Sei-Kei-Kakou 10 (3), 186–193 (in Japanese).
Tai, E., 1997. Polymer Camshaft, Trans. JSME 100 (942), 120 (in Japanese).